Indium and Tin Oxide Nanowires by Vapor-Liquid-Solid Growth Technique

PHO NGUYEN,[1] SREERAM VADDIRAJU,[1] and M. MEYYAPPAN[1,2]

1.—Center for Nanotechnology, NASA Ames Research Center, Moffett Field, CA 94035.
2.—E-mail: meyya@orbit.arc.nasa.gov

Regular three-dimensional (3-D) arrays of crystalline SnO_2–In_2O_3 nanowires were produced on m-sapphire using a gold catalyst-assisted vapor-liquid-solid growth process. The growth characteristics at multiple growth conditions were analyzed using scanning electron microscopy (SEM), transmission electron microscopy (TEM), selected area electron diffraction (SAED), x-ray photoemission spectroscopy (XPS), and Rutherford backscattering spectroscopy (RBS) to evaluate the functional dependence of nanowire structure and composition on growth parameters such as temperature and source composition. The results indicate that nanowires of mixed composition are not possible from the catalytic clusters; rather, a mixture of indium and tin oxide wires are formed in the range of conditions investigated here.

Key words: Inorganic nanowires, vapor-liquid-solid approach, tin oxide, indium oxide, catalyst-assisted growth

INTRODUCTION

Wide band-gap transparent metal oxide thin films[1–3] such as ZnO, ZrO_2, SnO_2, In_2O_3, and CdO are used in numerous applications ranging from energy storage/conversion, liquid crystal displays, gas sensors, electro-optic modulators, to microelectronics. Also, photonics[4] (i.e., optical waveguides and lasing devices) and field emission[5] applications of metal oxide micro and nano-structures have been reported in the literature. Recent advances in innovative device architecture enable incorporation of In_2O_3[6] and ZnO[7] nanowires as the semiconducting channels in field effect transistors and further demonstrate the multifunctionality of these metal oxide nanostructures. These potential applications have generated much interest in the synthesis and characterization of metal oxide nanowires of various compositions and desirable properties for use as functional components in logic circuitries, e.g., electrodes, channels in transistors, field emission and lasing components, and nanoscale sensing elements.[8–10] In this article, we explore the possibility of producing a high-density array of single-crystalline indium and tin oxide nanowires on optical m-sapphire and characterize their crystallographic properties.

(Received March 31, 2005; accepted September 22, 2005)

EXPERIMENTAL WORK

The synthesis approach involves a carbothermal reduction process followed by catalyst-assisted heteroepitaxial growth, using a previously reported reaction chamber setup.[11,12] The source consists of powder forms of indium oxide (In_2O_3, 99.999% purity), stannous tin oxide (SnO, 99.999% purity), and graphite (99.999% purity) in controlled mixture ratio. Stannous tin oxide is the material of choice due to its relative thermal and chemical volatility, compared to stannic tin oxide. The source is placed 2–3 cm upstream of the m-sapphire substrate inside a horizontal tubular reactor with an open egress. The substrate is coated with a 2-nm gold film using ion beam sputtering. The open egress design creates a relatively more oxidative environment for the formation of gas-phase metal oxides. Uniform arrays of tin oxide–indium oxide nanowires were successfully obtained at a constant argon carrier gas flow rate (Ar, 99.999%, 450 sccm), 800–900°C temperature window, and a growth time of 120 min. A parametric study varying the growth temperature and source composition was conducted.

RESULTS AND DISCUSSION

The dependence of morphology on temperature is studied first by fixing the source mixture ratio at 1:1:2 (In_2O_3:SnO:graphite) and varying the reaction temperature. Figures 1–3 depict scanning electron microscopy (SEM) images of arrays of $SnO_{2(x)}$–$In_2O_{3(y)}$ nanowires on m-sapphire substrates grown at 820°C, 850°C, and 880°C, respectively. As shown in Fig. 1a and b, the nanowires exhibit wirelike geometrical form with a relatively narrow diameter distribution of 59 nm ± 13 nm and an average length of ~6–8 μm. An intricate fabric of neatly fourfold symmetry forms on the m-sapphire substrate. Figure 1c shows a typical nanowire morphology: a smooth surface topography, a uniform diameter along the nanowire growth axis, and an oval-shaped catalytic nanoparticle at the terminating growth front, either slightly smaller or almost the same dimension as the nanowire diameter; all of these suggest adherence to the vapor-liquid-solid (VLS) mechanism.[13] The single crystallinity and growth direction of a representative nanowire are shown using high-resolution–transmission microscopy (HR–TEM) and selected area electron diffraction (SAED) (Fig. 1d and e). Well-defined lattice fringes of the (200) plane parallel to the growth front (2.36 Å), and a good match with the (200) plane spacing of tin (IV) oxide from x-ray powder diffraction (a = 4.737 Å and c = 3.186 Å, JCPDS 88–0287) are observed, suggesting the growth direction as [100]. As shown in Fig. 1e, a SAED pattern is resolved to confirm the [100] growth direction. For all conditions, HR–TEM analysis reveals well-defined lattice fringes traversing the entire width of the nanowire.

Structural characteristics of nanowires grown at 850°C are shown in Fig. 2. Figure 2a shows highly ordered array of fourfold symmetry of nanowires grown on m-sapphire with a diameter distribution of 81 nm ± 64 nm. The nanowires have a straight and smooth side-wall morphology with a nanoscale catalyst at the growth front. Figure 2d reveals the well-defined lattice fringes of the {200} family; the lattice fringes are perpendicular to the elongation plane, presenting [010], [101], or [011] as the growth directions. A SAED pattern is shown in Fig. 2e confirming the [011] growth direction and revealing the single crystallinity of the nanowire with its sharp diffraction spots.

At 880°C, two distinct nanostructures are discovered on the surface of the substrate. One morphology is a typical nanobelt structure with a large body (width ~177 nm ± 56 nm, thickness ~70 nm, and length ~3–4 μm) tapering to ~95 nm toward the growth front, with a catalyst head. The other chimera structure, which has never been reported previously, involves a nanobelt-like body (width ~180 nm ± 60 nm, thickness ~70 nm, and length ~2–3 μm) that terminates with a nanowire (diameter ~49 nm ± 52 nm and length ~2–3 μm) elongating at 45° of the growth direction of the belt; the junction is circled in Fig. 3a. The diameter of the nanowires is highly uniform and appears rather homogenous and free of observable domain defects/boundaries, suggesting high single crystallinity of these nanowires. The inset of Fig. 3a shows a bimodal distribution of diameters: the white bins denote the diameter distribution of the thinner nanowires and the dark bins represent the width of the nanobelts. In Fig. 3b, the HR–TEM image of the beltlike nanostructure shows

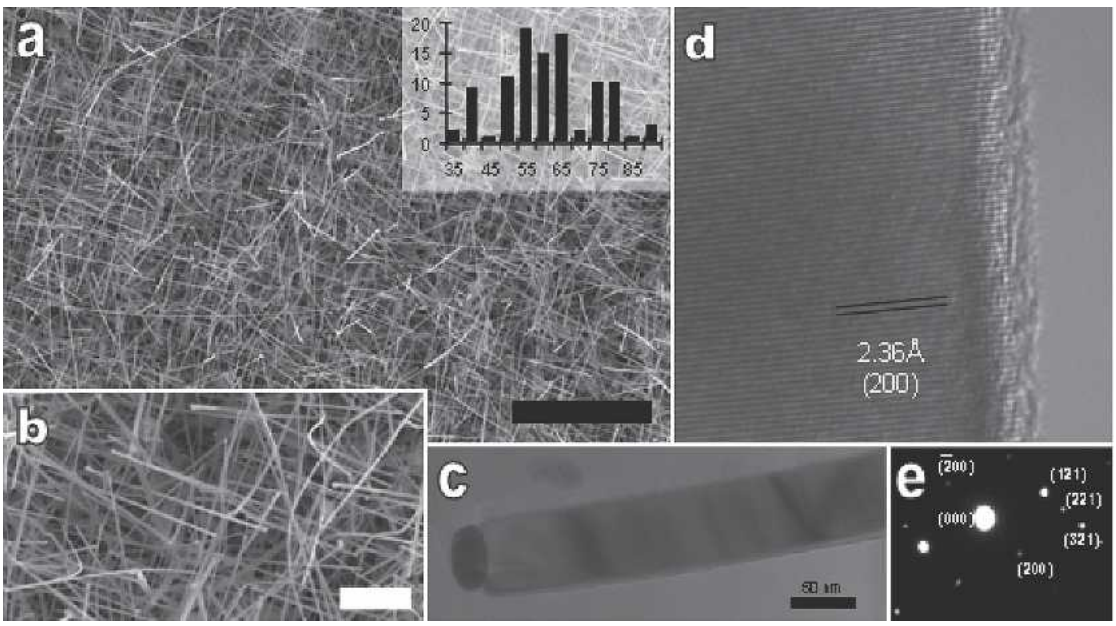

Fig. 1. Structural characterization of In_2O_3–SnO_2 nanowires on single crystalline optical m-sapphire substrates grown at 820°C. (a) and (b) Top-view SEM images of high-density regular arrays of nanowire (scale bar: 1 μm); the inset of (a) is a histogram of nanowire diameter distribution (in nanometers). (c) TEM image of the nanowire showing an oval catalyst head, smooth sidewall, and uniform diameter; some stress fringes are also observed. (d) HR–TEM showing the lattice fringes of the {200} family orthogonal to the growth direction, suggesting a [100] growth direction. (e) SAED pattern confirming the growth direction as [100].

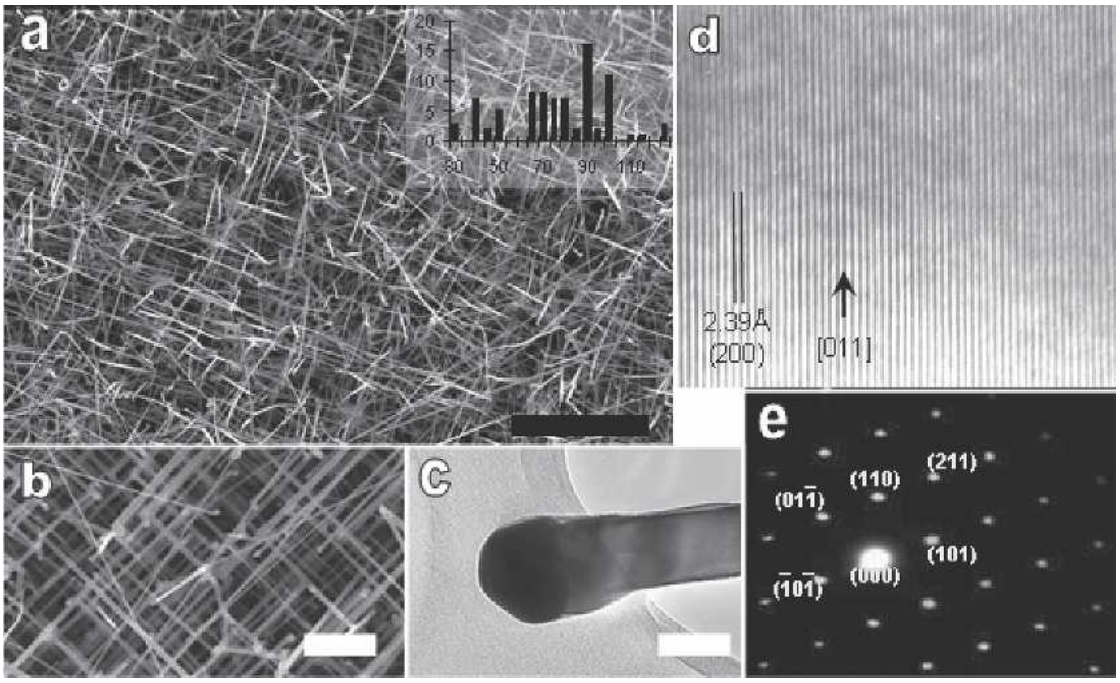

Fig. 2. Structural characterization of In_2O_3–SnO_2 nanowires on single crystalline optical m-sapphire substrates grown at 850°C. (a) and (b) Top-view SEM images of high-density regular arrays of nanowire (scale bar: 1 μm); the inset of (a) is a histogram of nanowire diameter distribution (in nanometers). (c) TEM image of the nanowire showing a polygonal catalyst head, smooth sidewall, and uniform diameter. (d) HR–TEM showing the lattice fringes of the {200} family parallel to the growth direction, suggesting a [011] growth direction. (e) SAED pattern confirming the growth direction as [011] and suggesting single crystallinity.

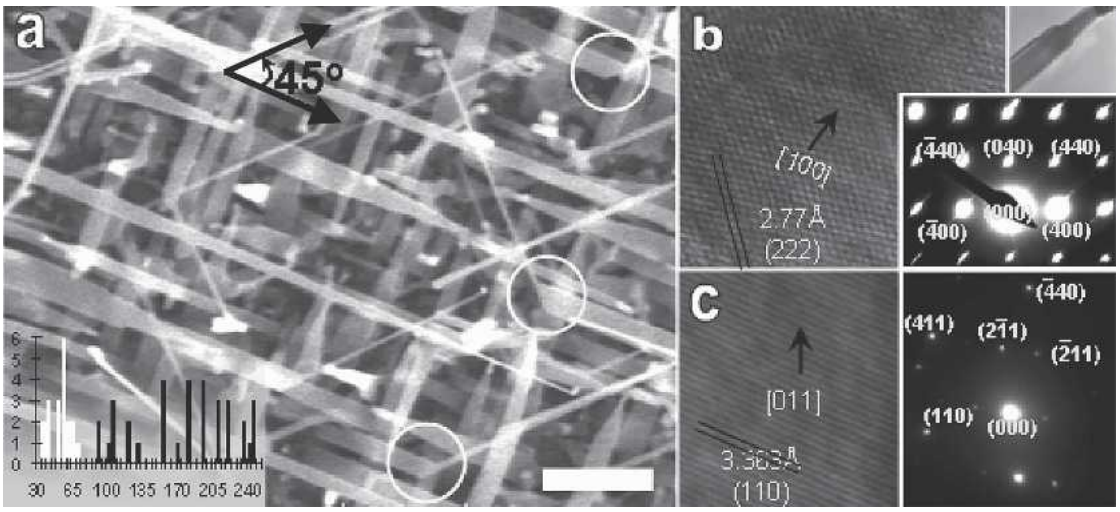

Fig. 3. Structural characterization of In_2O_3–SnO_2 nanowires on single crystalline optical m-sapphire substrates grown at 880°C. (a) Top-view SEM images of high-density regular arrays of nanowires and nanobelt (scale bar: 1 μm); the inset of (a) is a histogram of bimodal diameter distribution—white bins denote diameter distribution of the nanowire half and black bins represent the nanobelt half of the chimera structure. (b) HR–TEM image of the larger nanowire showing the lattice fringes of the (111) planes of indium oxide, suggesting a [100] growth direction; upper inset shows the corresponding nanobelt structure with a well-faceted hexagonal catalyst head; lower inset shows the diffraction pattern of the wire, confirming the structure of the nanobelt to be predominantly indium oxide with a growth direction of [100]. (c) HR–TEM image of the nanowire half showing the lattice fringes of the (110) planes of tin oxide, suggesting a [011] growth direction; inset shows the diffraction pattern of the wire, confirming the growth direction to be [011].

the (222) lattice fringes at 55° of the growth axis, indicating [100] as the growth direction. The corresponding SAED pattern shows the distinct pattern of indium (III) oxide and confirms the [100] growth orientation. The same diffraction pattern is recorded on the nanobelt half of the chimera structure. As shown on Fig. 3c, lattice fringes of the {110} plane family of tin (V) oxide, at 67° angle of the growth axis, are measured on the nanowire half of the chimera structure, indicating a [011] growth direction; and the resolved SAED pattern confirms the [011] growth direction of the tin oxide nanowire. A possible mechanism for chimera structure formation involves excessive vapor source generation at elevated temperature, followed by simultaneous physical deposition along the side walls of the

nanowire in preferred orientation, causing nanobelt formation.

Compositional analyses via x-ray photoemission spectroscopy (XPS) and Rutherford backscattering spectroscopy (RBS) are shown in Fig. 4. The XPS data show that the In_2O_3 molar percentage decreases from 8.7% ± 4.4% at 820°C to 4.9% ± 2.0% at 850°C, and to 4.1% ± 0.4% at 880°C; the range visualized in Fig. 4 denotes overlapping among datasets. Deconvolution of the Sn ($3d_{5/2}$), In ($3d_{5/2}$), and O (1s) peaks of the nanowires grown at various conditions (Fig. 5) reveals no distinct contributions due to metallic Sn and In in the respective spectra. The Sn ($3d_{5/2}$) peak is resolved to be only Sn^{4+} ions (487.5 eV) in SnO_2; no Sn^{2+} ion could be detected. Similarly, the In ($3d_{5/2}$) peak is deconvoluted into a single component: In_2O_3-like In (444.9 eV), surface hydroxide, or oxy-hydroxide species[14] peak is only occasionally observed. The asymmetric O (1s) peak has been deconvoluted into two major components: In_2O_3- (530.5 eV) and SnO_2- (531.0 eV) oxygen bond characteristics. A minor peak due to the hydroxyl and oxy-hydroxyl oxygen species, possibly, water and oxygen atoms that were physisorbed or chemisorbed[15–17] on the surfaces of the nanowires, is observed at 532.6 eV. A similar detailed discussion can be found elsewhere.[11] In summary, XPS analysis indicates the composition of the nanowires, grown at different temperatures using a 1:1:2 source mixture

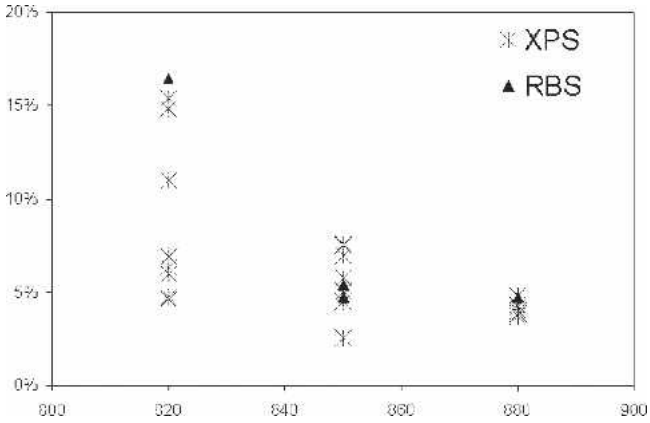

Fig. 4. Compositional analyses, via XPS and RBS, are performed. The XPS data show that the In_2O_3 molar percentage decreases from 8.7% ± 4.4% at 820°C to 4.9% ± 2.0% at 850°C, and to 4.1% ± 0.4% at 880°C. RBS concentration depth profiling of the nanowires, using a He^{++} ion beam of 2.275 MeV energy and 160° normal detection angle, demonstrates that the two measurement techniques, XPS and RBS, agree well with each other.

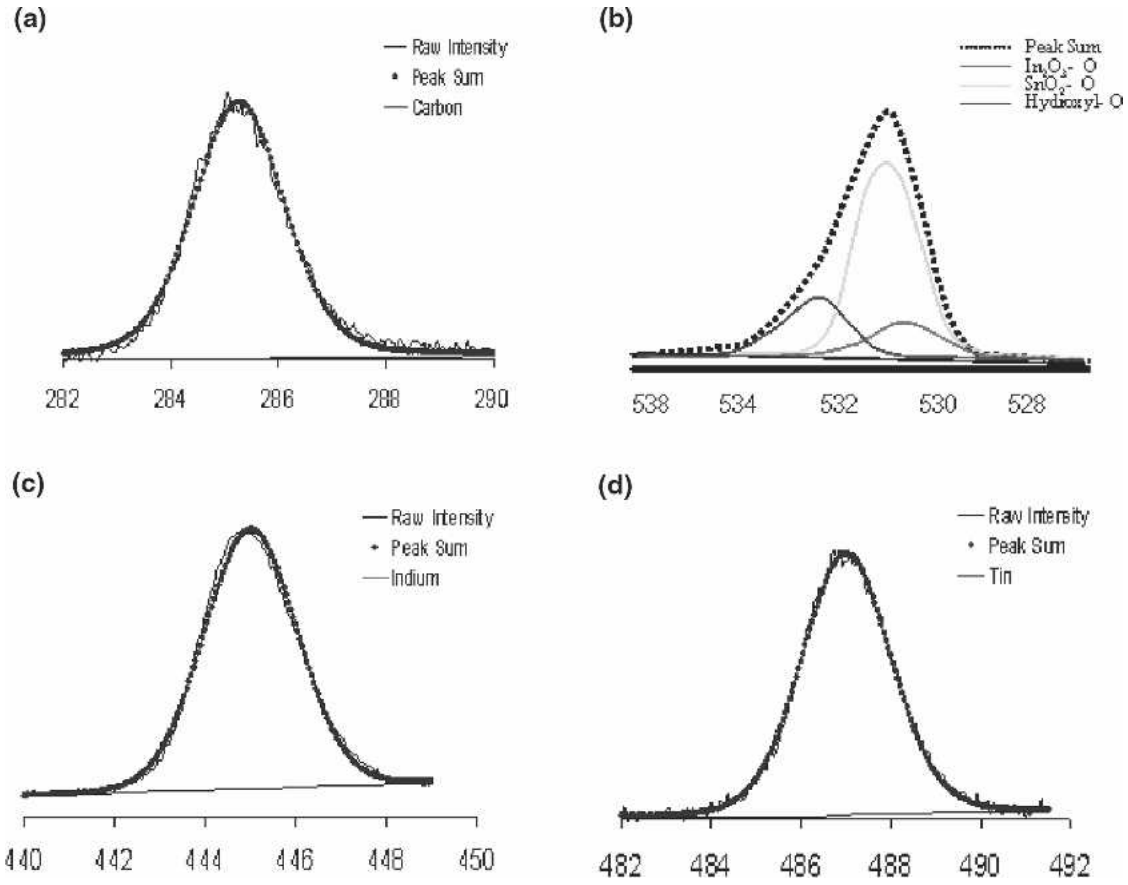

Fig. 5. Deconvolution of the Sn ($3d_{5/2}$), In ($3d_{5/2}$), and O (1s) XPS peaks of the nanowires grown at various conditions. Scale in x-axis is in eV. (a) Carbon peak at 284.6 eV is used to correct peak shifting. (b) Asymmetric O (1s) peak has been deconvoluted into two major and one minor component: In_2O_3-, SnO_2-, and hydroxyl oxygen bond characteristics, respectively. (c) In ($3d_{5/2}$) peak is deconvoluted into a single component of In^{3+} in In_2O_3; no metallic In is detected. (d) Sn ($3d_{5/2}$) peak is resolved to be only Sn^{4+} ions in SnO_2; no Sn^{2+} ion or metallic Sn could be detected. There are no other significant impurities detectable within the detection limits. A Shirley background correction was applied to each spectrum before the curve fitting. The extent of Gaussian–Lorentzian mixing was allowed to vary freely.

of tin oxide, indium oxide, and graphite powders, to be predominantly tin (IV) oxide and indium (III) oxide, the fully oxidized forms of indium and tin.

Since XPS has a penetration depth range of 50–100 Å and the nanowires have an average diameter in the range of 68–100 nm, we performed RBS concentration depth profiling (using a He^{++} ion beam of 2.275 MeV energy and 160° normal detection angle) to confirm the XPS data. Multiple measurement points, as shown on Fig. 4, demonstrate that the two measurement techniques agree well with each other. A representative RBS concentration depth profile is provided in Fig. 6, showing that indium-to-tin atomic ratio remains constant up to a calculated depth of 6 μm based on a thin film model. As shown in Figs. 1–3, 7, and 8, the intricate three-dimensional (3-D) nanowire fabric is highly porous; accordingly, actual penetration depth is likely deeper. The detection of hydrogen by RBS is consistent with XPS deconvolution of the oxygen peak.

The carbothermal reduction process generates liquid and vapor phases of the indium and tin species via the simplified set of reactions below:

$$SnO_{2(s)} + C_{(s)} \rightarrow Sn_{(s\rightarrow l\rightarrow g)} + CO_x$$

$$In_2O_{3(s)} + C_{(s)} \rightarrow In_{(s\rightarrow l\rightarrow g)} + CO_x$$

Using the Antoine equations to obtain the vapor pressures of indium and tin at the reaction temperatures,[17] it is observed that the In-Sn vapor pressure ratio decreases from 6,900 at 820°C, to 5,100 and 3,800 at 850°C and 880°C, respectively. This decrease suggests a rational correlation with the decreasing trend of the indium content in this temperature range. The fact that the nanowire matrix consists of predominantly tin oxide, when both In and Sn are present in the equal molar quantity at the source and indium oxide has a more negative $\Delta G_{formation}$, suggests that carbothermal decomposition and gas-phase formation of indium oxide proceed via a more tortuous pathway.[11]

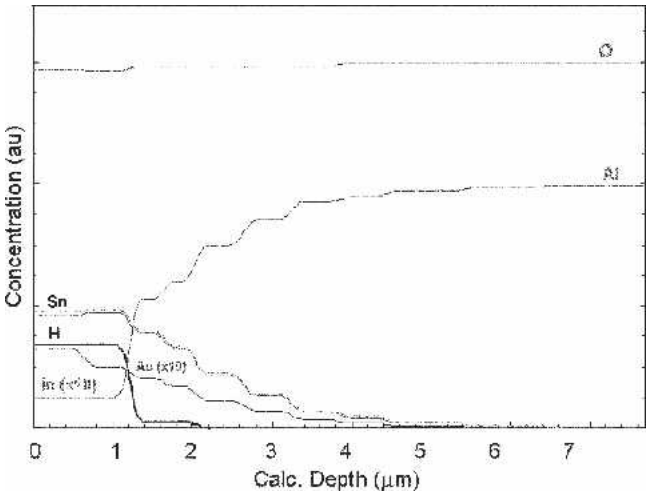

Fig. 6. RBS concentration depth profiling using a He^{++} ion beam of 2.275 MeV energy and 160° normal detection angle. The RBS spectra are fit by applying a theoretical model and iteratively adjusting elemental concentrations until good agreement is found between the theoretical curves and the respective experimental spectra. A representative RBS depth profile is provided here, showing that indium-to-tin atomic ratio remains constant up to a calculated depth of 6 μm based on a thin film model.

Alternatively, enhanced reactivity of the carbothermal reduction of tin oxide at the source is suggested as the driving force for the increase of tin oxide composition in the nanowires as the temperature is increased.

The second component of this study focuses on the growth characteristics as a function of the In_2O_3–SnO–graphite source preparation at a constant temperature of 850°C. The catalyst-assisted heteroepitaxial growth process allows intricate and complex cross-networks of uniform nanowires on m-sapphire substrates for the three mixing ratios 1:9:10, 1:1:2, and 9:1:10 (In_2O_3–SnO–graphite) investigated here. As shown in Figs. 7, 2, and 8, respectively, for these source mixtures, an ordered 3-D meshlike formation is seen with nanowires projecting mostly in directions orthogonal to each other and forming an intri-

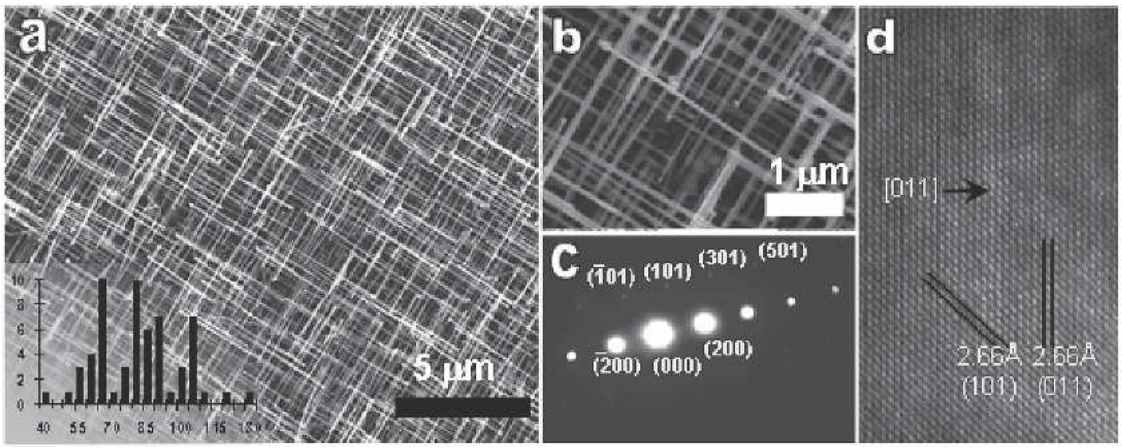

Fig. 7. Structural characterization of In_2O_3–SnO_2 nanowires on single crystalline optical m-sapphire substrate grown with indium oxide-tin oxide-graphite, source weight ratio of 1:9:10 at 850°C. (a) and (b) Top-view SEM images of high-density regular arrays of nanowires having fourfold symmetry. Inset of (a) shows the histogram of the diameter distribution (nanometers) with an average diameter and length of 78 nm ± 18 nm and 4–7 μm, respectively. (c) SAED pattern suggests the tetragonal structure of tin (IV) oxide and the [011] growth orientation. (d) HR-TEM micrograph of a nanowire confirms a growth direction of [011] with the lattice fringes of the (101) and (011) planes at 46° of each other.

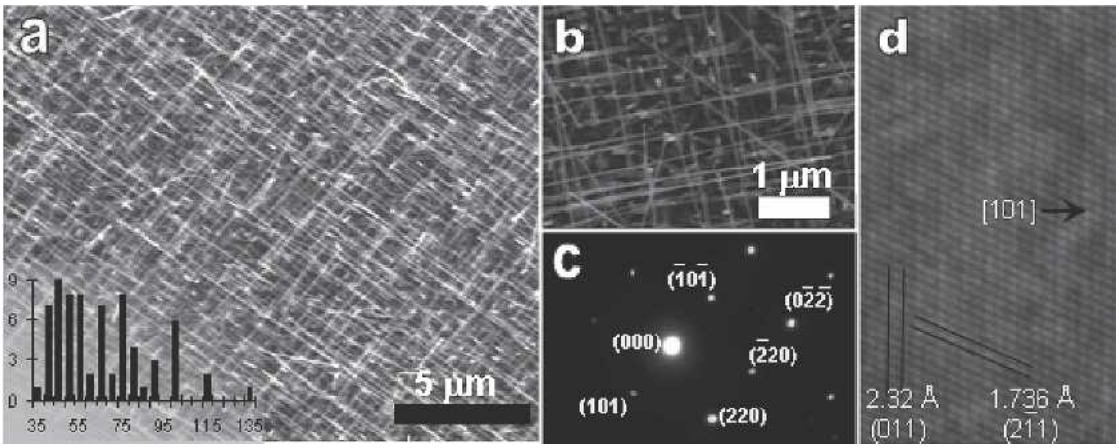

Fig. 8. (a) The In_2O_3–SnO–C mixing ratios of 9:1:10 at 850°C; the nanowire density markedly reduces and the average diameter decreases to 64 ± 21 nm. (b) Higher magnification shows the reduced density and nanowire diameter, as compared to Figs. 2b and 5b. (c) SAED pattern showing the diffraction spots of the {101} and {220} family. (d) HR–TEM micrograph showing lattice fringes of the (011) and (211) planes intersecting each other at 47°, with [101] as the growth direction.

cate fourfold symmetry. As shown in Fig. 7a and b, the 3-D network of nanowires grown with 1:9:10 source ratio has an average diameter and length of 78 nm ± 18 nm and 4–7 μm, respectively. The HR–TEM micrograph of a 1:9:10 nanowire demonstrates a growth direction of [011] with the lattice fringes of the (101) and (011) planes at 46° of each other (Fig. 7d). The corresponding SAED pattern (Fig. 7c) confirms the tetragonal structure of tin (IV) oxide and the [011] growth orientation as well.

Interestingly, for the In_2O_3–SnO–C mixing ratio of 9:1:10, the nanowire density markedly reduces and the average diameter decreases to 64 nm ± 21 nm, as shown in Fig. 8a and b. Figure 8c and d shows a HR–TEM micrograph and a SAED pattern of the thin wire. The HR–TEM micrograph reveals regular lattice fringes of the (011) and (211) planes intersecting each other at 47°, with [101] as the growth direction; this growth direction is also obtained by resolving the SAED pattern. In Fig. 9, the concentrations of indium oxide, obtained from XPS analysis, are 3.0 mol.% ± 0.6 mol.%, 4.8 mol.% ± 2.0 mol.%, and 4.7 mol.% ± 0.7 mol.%, respectively, for In_2O_3-SnO-C mixing ratios 1:9:10, 1:1:2, and 9:1:10.

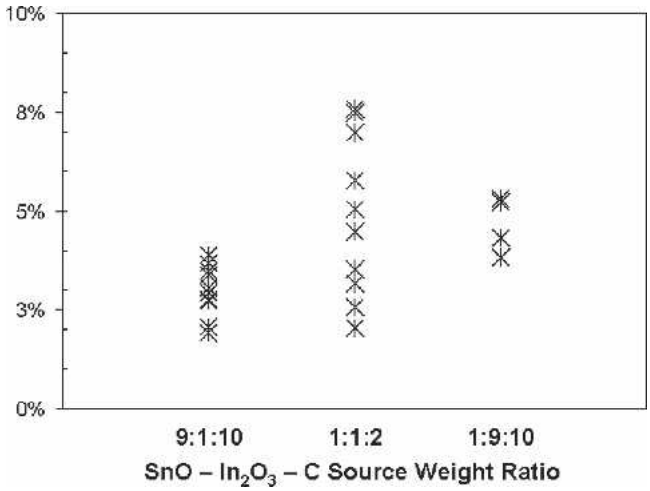

Fig. 9. Compositional analysis (showing molar percent of indium oxide) of the nanowires grown with various source weight ratios at 850°C using XPS.

CONCLUDING REMARKS

In the range of conditions investigated here, by varying the temperature and feed oxide mixture ratio, the result is a mixture of the two oxides and not a ternary alloy of indium and tin oxides. More characterization is needed to establish the local composition along the length of the wires to ascertain the formation of ternary alloys or indium (tin)–doped tin (indium) oxide wires. The VLS mechanism popularly known to produce one nanowire from one catalyst particle does not seem to yield nanowires with mixed oxide composition here even though, in principle, it might be possible. Yumoto et al.[18] reported formation of ITO whiskers using a VLS approach with an In:Sn atomic ratio of 54:46. One noticeable aspect of this work is that a self-catalytic process, with Sn particles serving as the template, yielded the ternary ITO whiskers. Then, it appears that a three-component system of In-Sn-O on Sn or In droplets is more amenable to grow ternary nanowires than a four-component system involving a foreign catalyst material (such as gold or a variety of other metals[19]), which requires a balanced diffusion of the two primary components into the particle.

ACKNOWLEDGEMENT

S. Vaddiraju is a Ph.D. candidate at the University of Louisville.

REFERENCES

1. J. McBreen, S. Srinivasan, A.C. Khandkar, and B.V. Tilak, *Electrode Materials and Process for Energy Conversions and Storage* (Pennington, NJ: Electrochemical Society, 1997).
2. V.G. Chigrinov, *Liquid Crystal Devices: Physics and Applications* (London: Artech House, 1999).
3. B. Cockayne and D.W. Jones, *Modern Oxide Materials: Preparation, Properties and Device Applications* (New York: Academic Press, 1972).
4. J.C. Johnson, H. Yan, R.D. Schaller, L.H. Haber, R.J. Saykally, and P. Yang, *J. Phys. Chem. B* 105, 11387 (2001).

5. H. Jia, Y. Zhang, X. Chen, J. Shu, X. Luo, Z. Zhang, and D. Yu, *Appl. Phys. Lett.* 82, 4146 (2003).
6. H.T. Ng, J. Han, T. Yamada, P. Nguyen, Y.P. Chen, and M. Meyyappan, *NanoLetter* 4, 1247 (2004)
7. P. Nguyen, H.T. Ng, T. Yamada, M.K. Smith, J. Li, J. Han, and M. Meyyappan, *NanoLetter* 4, 651 (2004).
8. A. Fang, H.T. Ng, and S.F.Y. Li, *Langmuir* 17, 4360 (2001).
9. L. Promsong and M. Sriyudthsak, *Sens. Actuat. B* 24–25, 504 (1995).
10. C. Li, D. Zhang, B. Lei, S. Han, X. Liu, and C. Zhou, *J. Phys. Chem. B* 107, 12451 (2003).
11. P. Nguyen, H.T. Ng, J. Kong, A.M. Cassell, R. Quinn, J. Li, J. Han, M. McNeil, and M. Meyyappan, *Nano Lett.* 3, 925 (2003).
12. P. Nguyen (Master's Thesis, San José State University, 2003).
13. R.S. Wagner and W.C. Ellis, *Appl. Phys. Lett.* 4, 89 (1964).
14. C. Donley, D. Dunphy, D. Paine, C. Carter, K. Nebesny, P. Lee, D. Alloway, and N.R. Armstrong, *Langmuir* 18, 450 (2002).
15. I.S. Mulla, V.J. Rao, H.S. Soni, S. Badrinarayanan, and A.P.B. Sinha, *Surf. Coating Technol.* 31, 77 (1987).
16. B. Yea, H. Sasaki, T. Osaki, K. Sugahara, and R. Konishi, *Jpn. J. Appl. Phys.* 38, 2103 (1999).
17. D.R. Lide, editor, *CRC Handbook of Chemistry and Physics*, 78th ed. (Boca Raton, FL: CRC Press, 1998).
18. H. Yumoto, T. Sako, Y. Gotoh, K. Nishiyama, and T. Kaneko, *J. Cryst. Growth* 203, 136 (1999).
19. P. Nguyen, H.T. Ng, and M. Meyyappan, *Adv. Mater.* 17, 1773 (2005).